How to cite: *Angew. Chem. Int. Ed.* **2022,** *61,* e202213773
International Edition: doi.org/10.1002/anie.202213773
German Edition: doi.org/10.1002/ange.202213773

Zeolite Nanosheets

Amorphous Aluminosilicate Nanosheets as Universal Precursors for the Synthesis of Diverse Zeolite Nanosheets for Polymer-Cracking Reactions

Koki Sasaki, Jose A. Hernandez Gaitan, Tsuyoshi Okue, Shotaro Matoba, Yuki Tokuda, Koji Miyake, Yoshiaki Uchida, and Norikazu Nishiyama*

Abstract: Zeolites catalyze some reactions in their molecular-sized pores, but large molecules can react only on their external surface. Zeolite-nanosheets (NSs) have been developed as catalysts for large molecules. The previously reported methods to synthesize zeolite-NSs are specialized for each zeolite type. Here we propose a new method to synthesize various zeolite-NSs from the same amorphous aluminosilicate NSs (AAS-NSs) as a universal precursor. We successfully synthesized the unprecedented AAS-NSs in the hydrophilic space of the stable hyperswollen lyotropic lamellar (HL) phase. The four zeolite types could be obtained from the single-species AAS-NSs. These results imply that this method enables us to synthesize almost all types of zeolite-NSs. Moreover, the synthesized CHA-NSs have great potential for various applications because of their thickness and large external surface area.

Introduction

Zeolites are crystalline aluminosilicates with molecular-sized pores (0.3–1.2 nm diameter). The porous structures lead to unique functions: catalysts, catalyst supports, adsorbents, ion-exchangers, membranes and membrane reactors. Therefore, various zeolites tailor-made for each application have been artificially synthesized.[1] One of the uses of some zeolites with strong Brønsted acid sites like CHA-type zeolites is to catalyze cracking reactions that are indispensable for petrochemical industries. The cracking of waste polymers could make recycled monomers desirable in green chemistry and SDGs;[2] however, polymers are too large to react in the pores of such zeolites, and the reaction occurs only on the external surfaces of zeolites. Large external specific surface area (S_{ext}) contributes to the increase of the reaction rates of the polymer cracking.[3] To increase S_{ext}, the downsizing of the zeolite crystals is effective; zeolite nanoparticles,[4] nanowires[5] and nanosheets (NSs)[6] generally catalyze the reactions of large molecules better than the corresponding bulk crystals.[7,8]

The synthesis method of the zeolite-NSs has been developed according to the feature of each crystal structure. The first-generation strategy of the zeolite-NSs synthesis is the exfoliation of layered zeolites.[9,10] Whereas the first zeolite-NS, ITQ-2, was synthesized by exfoliating an MWW-type zeolite,[6] this method could not apply to most other non-exfoliable zeolites. The second-generation strategy is anisotropic crystal growth. It uses the difference in the growth rates of crystal planes.[11–19] Some zeolite-NSs with anisotropic crystal structures can be obtained in the hydrothermal (HT) treatments using amphiphilic growth inhibitors that covalently bind structure-directing moieties. The amphiphilic moiety inhibits the growth of a specific crystal plane, and the structure-directing moiety decides the crystal structures. Meanwhile, the NSs synthesis of zeolites with cubic or pseudo-cubic lattices showing isotropic growth needs another appropriate method.

To synthesize zeolite-NSs, one must control two aspects: external shape and crystal structure. We conceived the two-step procedure to make the former and latter sequentially, as shown in Figure 1. The first step is an anisotropic growth of isotropic amorphous aluminosilicate (AAS) to give AAS-NSs as a universal precursor of zeolite-NSs. The second step is converting it to zeolite-NSs using commonly used structure-directing agents (SDAs). Zeolite-NSs have to be prevented from aggregating during the second step. As a synthesis method of amorphous NSs, the "two-dimensional reactor in amphiphilic phases (TRAP) method" is useful.[20–25] Hyperswollen lyotropic lamellar (HL) phases, consisting of many bilayers with several nm thicknesses, work as independent TRAPs for amorphous NSs.[26] The TRAPs prevent NSs from aggregating because they keep several hundred nm intervals. The crystallization methods of AAS to zeolites are divided into HT and dry gel conversion (DGC) methods. The latter crystallizes AAS in the steam treatment,[27] and it can better suppress the aggregation of zeolite particles than the former.[28]

Here, we report the effects of the increase of S_{ext} on the cracking reactions of low-density polyethylene (LDPE) with

[*] K. Sasaki, J. A. H. Gaitan, T. Okue, S. Matoba, Y. Tokuda, K. Miyake, Y. Uchida, N. Nishiyama
Graduate School of Engineering Science, Osaka University
1–3 Machikaneyama, Toyonaka, Osaka, 560-8531 (Japan)
E-mail: y.uchida.es@osaka-u.se.jp

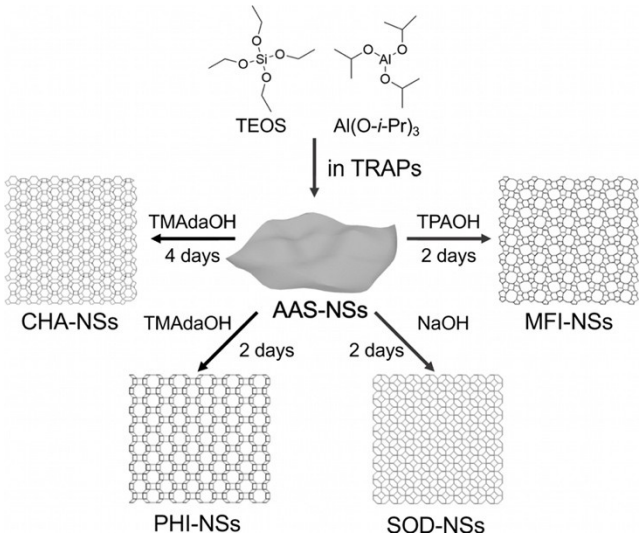

Figure 1. Schematic illustration of the synthesis procedure for the zeolite-NSs. We synthesize AAS-NSs as the universal precursor for defining the external shape of zeolite-NSs. And then, we crystallize AAS-NSs to zeolite-NSs using the DGC method without changing the NS shape.

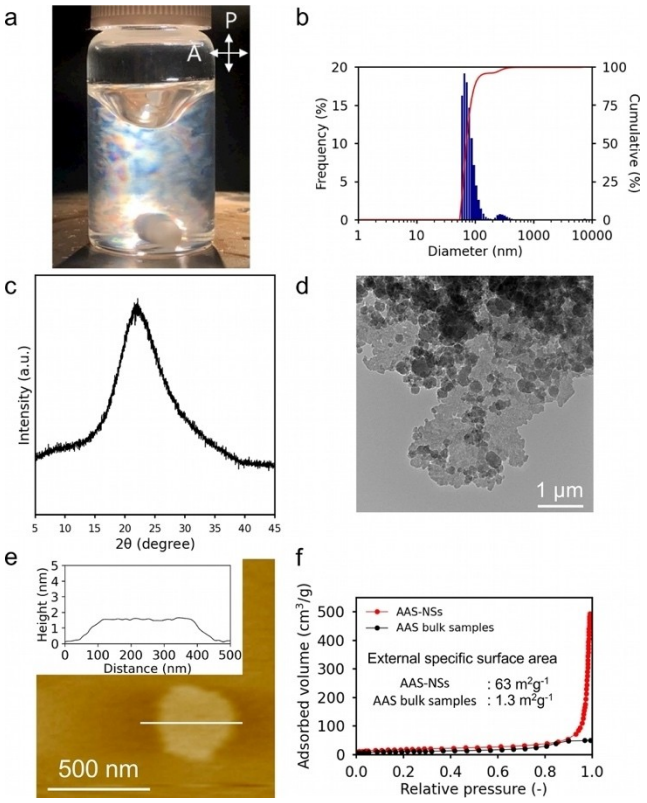

Figure 2. Reaction conditions and characterization of obtained AAS-NSs. a) Liquid crystalline texture of the hyperswollen lyotropic lamellar phase of a decane solution of SOBS (0.95 wt%), 1-pentanol (8.4 wt%), and water (1.1 wt%) with NaOH (9.4×10^{-3} wt%), TEOS (0.25 wt%) and Al(O-*i*-Pr)$_3$ (1.2×10^{-2} wt%) at 60 °C. Samples are placed between crossed polarizers. b) DLS analysis of AAS-NSs dispersed in the TRAP solutions. c) XRD pattern of the AAS-NSs. d) TEM photograph of one of the synthesized AAS-NSs. e) AFM photograph and cross-section of one of the synthesized AAS-NSs. f) Nitrogen adsorption isotherms of AAS-NSs and AAS bulk samples.

the unprecedented CHA-type zeolite-NSs (CHA-NSs) synthesized from the AAS-NSs as the universal precursor that we synthesized inside the hydrophilic TRAPs in a decane solution of an amphiphile. We also discuss the retention of the external shapes during the DGC method from the AAS-NSs to CHA-NSs. Moreover, we synthesized SOD-type and MFI-type zeolite-NSs (SOD-NSs and MFI-NSs) as other examples to demonstrate the universality of the two-step method. Besides, we demonstrate the performance of the SOD-NSs and MFI-NSs as acid catalysts.

Results and Discussion

We synthesized AAS-NSs in an HL phase with hydrophilic TRAPs consisting of sodium *p*-octylbenzenesulfonate (SOBS). First, we confirmed the stability of the HL phases against the presence of the ingredients of AAS.[23,24] Hydrophobic ingredients, tetraethyl orthosilicate (TEOS) and aluminum isopropoxide (Al(O-*i*-Pr)$_3$), and hydrophilic ingredients, sodium hydroxide (NaOH) and water, can be dissolved in the TRAP solution and do not affect the stability of the HL phases, as shown in Figure 2a and Figure S1. After stirring the reaction mixture for 24 h at 60 °C, we obtained a suspension of the products, which still showed an HL phase. We estimated the particle size distributions of the products in the TRAPs by using a dynamic light scattering (DLS) method. The suspension contained few aggregates, as shown in Figure 2b.

Then, we centrifugated the reaction mixture, washed the obtained white powder with methanol, and dried it. Its X-ray diffraction (XRD) pattern shows only one broad peak around $2\theta = 15$–$30°$, as shown in Figure 2c. Therefore, the obtained powder seems amorphous. The transmission electron microscopy (TEM) photographs for the powder indicate that it consists of NSs, as shown in Figure 2d. We measured the thickness and horizontal width of the NSs to be 1.96 ± 0.67 nm and 395 ± 137 nm, respectively, using atomic force microscopy (AFM), as shown in Figure 2e. The nitrogen adsorption results indicate that the S_{ext} of AAS-NSs was larger than that of AAS bulk samples, as shown in Figure 2f and Table S1, respectively. The scanning electron microscope-energy dispersive X-ray spectroscopy (SEM-EDX) of the NSs suggests the presence of silicon, aluminum, sodium and oxygen, as shown in Figure S2. Sulfur from the amphiphilic SOBS was absent. We can conclude that the hydrophilic TRAP method synthesizes AAS-NSs using not chemical inhibition of the particle growth but physical confinement.[23] However, removing SOBS was likely to induce the aggregation of AAS-NSs, as shown in Figure S3. The crystallization of the AAS-NSs without SOBS in the DGC process gave large particles, as shown in Figure S4.

We examine if SOBS inhibits the aggregation of NSs as a dispersant for AAS-NSs in the DGC process. The first step of the DGC process is the preparation of the dry gels of

AAS-NSs. To obtain the AAS-NSs coated with SOBS, we added ethanol to the TRAP solution instead of methanol in the purification process of the synthesized AAS-NSs. Because SOBS is insoluble in ethanol, adding ethanol destabilized the HL phase, and the SOBS precipitated with AAS-NSs. We did the centrifugal separation of the solution and obtained AAS-NSs. The SEM-EDX of the AAS-NSs suggests the presence of sulfur, as shown in Figure S5. The AAS-NSs were probably coated with SOBS.

Next, we should confirm whether SOBS works as a dispersant in the DGC process to give CHA-type zeolites. The coated AAS-NSs were soaked in the aqueous solutions of *N*,*N*,*N*-trimethyladamantan-1-aminium hydroxide (TMAdaOH), which is a typical SDA to synthesize CHA-type zeolites. After drying the mixture at 90 °C, the dried precursor gel was put in a Teflon-lined stainless-steel autoclave with water separately, where the reaction took place with the steam produced at 160 °C for 96 h. The product was washed with water, dried, calcinated and purified by filtration to give a white powder. Its XRD pattern is typical of CHA structures, as shown in Figure 3a.

Meanwhile, the powder obtained after 48 h crystallization exhibited an XRD pattern typical of PHI structures, as shown in Figure S6a. These results suggest that AAS-NSs were transformed into a PHI-type zeolite and were further transformed into a CHA-type zeolite.[29] This type of polymorphic transition often occurs for bulk zeolites. The full width at half maximum (FWHM) of each XRD peak for the obtained CHA crystals was broader than that of conventional CHA crystals, as shown in Table S2. The FWHM of each of the XRD peaks for the obtained PHI crystals was also broader than that of conventional PHI crystals, as shown in Table S3. These results also show that the growth inhibition of a certain crystal plane does not occur. The Williamson-Hall plots shown in Figures S7 and S8 indicate that the crystallite size of the obtained powder is smaller than that of conventional zeolite crystals.[30]

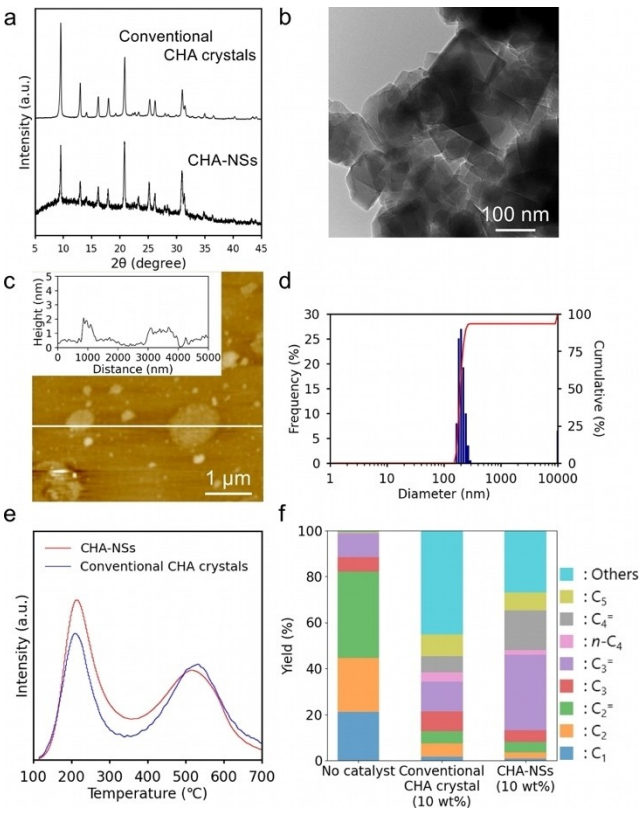

Figure 3. Characterization of the synthesized CHA-NSs. a) XRD pattern of the CHA-NSs. b) TEM photograph of one of the synthesized CHA-NSs. c) AFM photograph and cross-section of one of the synthesized CHA-NSs. d) DLS analysis of the CHA-NSs. e) NH_3-TPD profiles of the CHA-NSs after filtration and conventional CHA crystals. f) Product distribution in LDPE cracking reaction of no catalyst, conventional CHA crystals (10 wt%), and CHA-NSs (10 wt%).

The TEM photographs for the PHI-type and CHA-type zeolites exhibit NSs similar to the AAS-NSs, as shown in Figures 3b, S6b, S9a–S9c, and S10a–S10c. The selected area electron diffraction (SAED) patterns for the PHI-type zeolite-NSs (PHI-NSs) and CHA-NSs indicate that they are polycrystals consisting of small crystals; each shows concentric circles, as shown in Figures S9e and S10e. We measured the thickness and horizontal width of the PHI-NSs to be 2.20 ± 1.08 nm and 416 ± 241 nm, respectively, and those of the CHA-NSs to be 2.13 ± 0.60 nm and 528 ± 106 nm, respectively, using AFM, as shown in Figures 3c, S6c, S9f, S9g and S10f–S10j. We measured 15 NSs and calculated the average and standard deviation of the size and thickness. When we prepared the sample for AFM, the ethanol suspension was dripped onto the substrates, and the suspension was sucked out. The sucking process was not applied for TEM. Therefore, we could prevent NSs from aggregation and observe the unstacked NSs using AFM. The round shape of observed NSs in AFM images looks different from the angular shape of NSs in TEM images. It perhaps comes from the difference in the observation method that the amorphous sites at the edges can disappear in TEM because amorphous sites are particularly sensitive to electron beams.[31] We can observe the cracking and shape deformation of CHA-NSs during TEM observation. After filtration, we estimated the particle size distributions of the PHI-NSs and CHA-NSs by DLS measurements. These results suggest the absence of the aggregates, as shown in Figures 3d and S6d. The SEM-EDX spectra of the CHA-NSs and PHI-NSs indicate that Si/Al ratio is about 9 and 3, as shown in Figures S11 and S12, respectively. These results indicate that SOBS prevents AAS-NSs from deformation and aggregation during the DGC process.

To estimate the amount of Brønsted acid sites of the CHA-NSs, we measured ammonia's temperature-programmed deposition (NH_3-TPD) patterns for the synthesized CHA-NSs and conventional CHA crystals. The NH_3-TPD patterns have two peaks; the higher temperature peak corresponds to the amount of Brønsted acid sites.[32] As shown in Figure 3e, the amount of Brønsted acid sites for the CHA-NSs was estimated to be $0.230\ mmol\,g^{-1}$, nearly equal to that for the conventional CHA crystals ($0.257\ mmol\,g^{-1}$). The higher temperature peak for the CHA-NSs is smaller than that of the conventional crystals. These results imply that the crystallinity of the CHA-NSs is

lower than the conventional CHA crystals. The Williamson-hall plot for the CHA-NSs suggests that the NSs grow as a collection of small crystals with various orientations, as shown in Figure S7. These results indicate that the crystallization begins at some points in the same NS, and each crystallite grows individually in size and direction. It should result in the residual amorphous sites at the boundaries between the crystallites, as shown in Figure S13. Field emission transmission electron microscopy (FE-TEM) also supports it; the smaller crystallites increase the volume of amorphous sites in their interstitial spaces, as shown in Figure S14.

Moreover, the higher temperature peak for the CHA-NSs is on the lower temperature side than that of the conventional CHA crystals. It is because the desorption energy for the external surface is lower than that for the internal surface in the pores. There are probably more Brønsted acid sites at the external surface for the CHA-NSs.[33] To evaluate the S_{ext}, we measured the nitrogen adsorption for both samples. The S_{ext} of the CHA-NSs was larger than that of conventional CHA crystals, as shown in Table 1 and Figure S15, respectively. This result is consistent with the above expectation for the Brønsted acid sites at the external surface. The CHA-NSs probably have many Brønsted acid sites at the external surface.

We also measured the NH_3-TPD patterns for the PHI-NSs and conventional PHI crystals, as shown in Figure S16. The PHI-NSs have Brønsted acid sites ($0.186\,mmol\,g^{-1}$), while the conventional PHI crystals have few Brønsted acid sites ($0.003\,mmol\,g^{-1}$). The remarkable difference should be attributed to a cage in the PHI-type structure. The conventional PHI crystals contain sodium and potassium ions as counter cations, as shown in Figure S12a. It suggests that the ions in the cages cannot leave, and ammonium ions cannot enter the cages because their pore size is smaller than the ion. It is consistent with the NH_3-TPD pattern. Meanwhile, some PHI-NSs contain fewer counter cations, as shown in Figure S12b. Whereas the unit size of PHI-type zeolite is $0.98\,nm \times 1.41\,nm \times 1.40\,nm$, the thickness of the synthesized PHI-NSs is about 2.2 nm. Therefore, the cage of the PHI-NSs seems to be exposed on the surface. Because the PHI-NSs have exchangeable counter cations, ammonium ions can reach the acid sites.

Table 1: Specific surface area (S_{total}), external surface area (S_{ext}), and pore volume (V_{total}) of conventional CHA crystals, CHA-NSs before filtration, and CHA-NSs after filtration measured by nitrogen adsorption isotherms.

	S_{total}[a] $[m^2\,g^{-1}]$	S_{ext}[b] $[m^2\,g^{-1}]$	V_{total}[b] $[cm^3\,g^{-1}]$
Conventional CHA crystals	820	7.5	0.30
CHA-NSs before filtration	635	22.6	0.22
CHA-NSs after filtration	260	51	0.06

[a] Surface area calculated using BET method (BET surface area) applied to the nitrogen adsorption isotherm. [b] S_{ext} and V_{total} calculated using the *t*-plot method applied to the nitrogen adsorption isotherm.

To evaluate the S_{ext}, we measured the nitrogen adsorption for both samples. The S_{ext} and the specific surface area (S_{total}) of the PHI-NSs were also larger than those of conventional PHI crystals, as shown in Figure S17 and Table S4. Although the nitrogen molecule is hardly adsorbed on PHI-type zeolites,[34] it was adsorbed on the PHI-NSs. It also indicates that the cages are exposed to the surface.

We did an acid-catalyzed LDPE cracking test, which was thought to be a suitable probe reaction for diffusion-limited reactions, to evaluate the activity of the prepared CHA and PHI-type zeolites, as shown in Figure S18. We prepared the LDPE samples with 10 wt % of the CHA-NSs, conventional CHA crystals, the PHI-NSs, or conventional PHI crystals. The products of the LDPE cracking test are shown in Figures 3f, and S20a, and Tables S5 and S6. We compare the yield of products smaller than pentane because it is difficult to distinguish olefin and paraffin larger than pentane. These results show that adding zeolites increases the selectivity of the lower olefins, as shown in Figures 3f, S19, and S20b and Tables S5 and S6. The CHA-NSs and PHI-NSs raise the ratio of lower olefine more than the same amount of conventional CHA and PHI crystals, respectively. The improved accessibility of the Brønsted acid sites at the external surfaces positively influences the cracking performance. Therefore, we could conclude that an increase in S_{ext} promotes LDPE cracking.

To prove that the AAS-NSs can be transformed into the zeolite-NSs with cubic lattice as a universal precursor, we also synthesized SOD-NSs. The AAS-NSs were soaked in NaOH solution, and we obtained the dried precursor gel after drying the solution. After the DGC process at 180 °C for 48 h, we collected a white powder. Its XRD pattern suggests that the AAS-NSs transformed into SOD-type structure, as shown in Figure 4a.[35] The FWHMs and the Williamson-Hall plots shown in Table S7 and Figure S21, respectively, indicate that the crystallite size of the obtained powder is smaller than that of the conventional SOD crystals. The TEM photographs for the white powder exhibit discrete NSs similar to the AAS-NSs, as shown in Figures 4b and S22a–S22c. The SAED pattern for the SOD-NSs indicates that they are polycrystals consisting of small crystals; it shows concentric circles, as shown in Figure S22e. We measured the thickness and horizontal width of the white powder to be 2.13 ± 0.18 nm and 219 ± 24 nm by AFM, respectively, as shown in Figures 4c and S22f and S22g. We measured 15 NSs and calculated the average and standard deviation of the size and thickness, respectively. After filtration, we estimated the particle size distributions by DLS measurements of the SOD-NSs. It suggests the absence of the aggregates, as shown in Figure 4d. The SEM-EDX spectra of conventional SOD crystals and the SOD-NSs indicate that Si/Al ratio is about 1 and 2, respectively, as shown in Figure S23. These results indicate that this method synthesizes the zeolite-NSs with cubic lattice.

We also measured the NH_3-TPD patterns for the SOD-NSs and conventional SOD crystals, as shown in Figure S24. The SOD-NSs have Brønsted acid sites ($0.012\,mmol\,g^{-1}$), while the conventional SOD crystals have few Brønsted acid

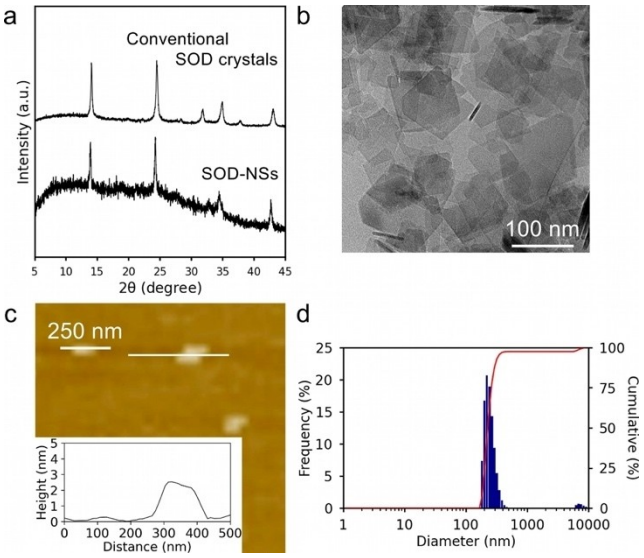

Figure 4. Characterization of the synthesized SOD-NSs. a) XRD pattern of the SOD-NSs. b) TEM photograph of one of the synthesized SOD-NSs. c) AFM photograph and cross-section of the synthesized SOD-NSs. d) DLS analysis of the SOD-NSs.

sites (0.004 mmol g^{-1}). The difference is much smaller than that between the PHI conventional crystals and the PHI-NSs. The conventional SOD crystals contain sodium ions as counter cations, as shown in Figure S23a. Whereas the unit size of SOD-type zeolite is 0.90 nm × 0.90 nm × 0.90 nm, the thickness of the synthesized SOD-NSs is about 2.1 nm. The fewer cages of the SOD-NSs should be exposed on the surface than the PHI-NSs. It should lead to less acidity than the PHI-NSs.

We measured the nitrogen adsorption for both samples to discuss the difference between the SOD-NSs and PHI-NSs. The S_{ext} of the SOD-NSs was larger than those of conventional SOD crystals like the PHI-NSs, as shown in Figure S25 and Table S8, respectively. However, the S_{total} of the SOD-NSs was much smaller than the PHI-NSs. The nitrogen adsorption isotherm shows that the SOD-NSs have micro pores larger than nitrogen molecules. However, the nitrogen molecule was hardly adsorbed in the cages of SOD-type zeolite. It supports that the fewer cages of the SOD-NSs should be exposed on the surface than the PHI-NSs.

The residual counter ions should deactivate the SOD-NSs as an acid catalyst. To confirm the hypothesis, we did an acid-catalyzed LDPE cracking test for the SOD zeolites. When we prepared the LDPE samples with 10 wt % of the SOD-NSs or conventional SOD crystals, these two samples showed almost the same results as the LDPE without any zeolites, as shown in Figure S26 and Table S9. It is conclusive that the SOD-NSs have very few Brønsted acid sites, as with usual SOD-type zeolites.

We examine if the AAS-NSs can be transformed into the zeolite-NSs the second-generation strategy has already synthesized;[11] we synthesized MFI-NSs. The obtained AAS-NSs were soaked in tetrapropylammonium hydroxide (TPAOH) solution, and we obtained the dried precursor gel after drying the solution. After the DGC process at 180 °C for 48 h, we collected a white powder. Its XRD pattern suggests that the AAS-NSs transformed into an MFI-type structure, as shown in Figure 5a.[36] The FWHMs and the Williamson-Hall plots shown in Table S10 and Figure S27, respectively, indicate that the crystallite size of the obtained powder is smaller than that of conventional MFI crystals. The TEM photographs for the white powder exhibit discrete NSs similar to the AAS-NSs, as shown in Figures 5b and S28a–S28c. The SAED pattern for the MFI-NSs indicates that they are polycrystals consisting of small crystals; it shows concentric circles, as shown in Figure S28e. We measured the thickness and horizontal width of the white powder to be 1.49 ± 0.17 nm and 580 ± 150 nm by AFM, respectively, as shown in Figures 5c, S28f and S28g. We measured 15 NSs and calculated the average and standard deviation of the size and thickness. After filtration, we estimated the particle size distributions by DLS measurements of the MFI-NSs. It suggests the absence of the aggregates, as shown in Figure 5d. These results indicate that this method synthesizes the zeolite-NSs with anisotropic crystal structures.

The SEM-EDX spectra of conventional MFI crystals and the MFI-NSs indicate that Si/Al ratio is about 10 and 6, respectively, as shown in Figure S29. Since the Si/Al ratio of the MFI-NSs is quite lower than the usual MFI-type zeolites, aluminum atoms are probably concentrated in the amorphous regions. Therefore, the crystallinity of the MFI-NSs is lower than that of the CHA-NSs, as shown in Figures 3a and 5a. Besides, we measured NH_3-TPD patterns for the synthesized MFI-NSs and conventional MFI crystals. The amount of Brønsted acid sites for the MFI-NSs was estimated to be 0.059 mmol g^{-1}, much lower than that for the conventional MFI crystals (0.349 mmol g^{-1}), as shown in

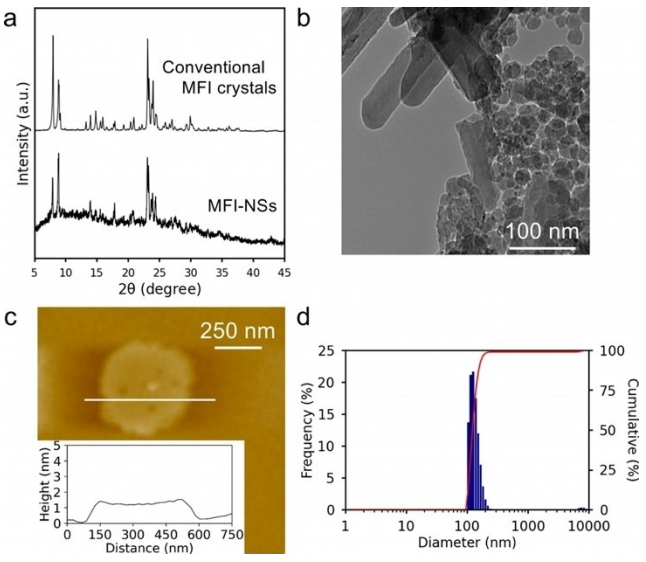

Figure 5. Characterization of the synthesized MFI-NSs. a) XRD pattern of the MFI-NSs. b) TEM photograph of one of the synthesized MFI-NSs. c) AFM photograph and cross-section of one of the synthesized MFI-NSs. d) DLS analysis of the MFI-NSs.

Figure S30. We also measured the nitrogen adsorption for both samples. The S_{ext} of the MFI-NSs was larger than that of conventional MFI crystals, as shown in Figure S31 and Table S11. The MFI-NSs probably have many Brønsted acid sites at the external surface.

We did an acid-catalyzed LDPE cracking test. We prepared the LDPE samples with 10 wt % of the MFI-NSs or conventional MFI crystals. The LDPE cracking test shows that adding the MFI-type zeolites increases the selectivity of the lower olefins, as shown in Figure S32 and Table S12. The effect of adding the MFI-NSs was almost the same as conventional MFI crystals. The effect of the expansion of S_{ext} is small because the same reactions occur inside and outside the pores. Even though MFI-type zeolite has weaker acidity than CHA-type, coke production occurs more in the MFI-NSs than the CHA-NSs, as shown in Figure S33. The CHA-NSs produced other volatile components more than MFI-type, which are likely longer alkanes or alkenes. These results are attributed to the larger pores of MFI-type zeolites than that of CHA and PHI-type zeolites. It supports that the CHA-NSs react with the LDPE on their external surfaces, whereas the MFI-NSs react with LDPE both on their external surface and in the pores.

Conclusion

We have demonstrated a new method to synthesize various zeolite-NSs from single-species AAS-NSs prepared by the TRAP method. We successfully synthesized the unprecedented AAS-NSs by TRAP methods and the four zeolite types from single-species AAS-NSs by DGC process with SDAs. The coating with SOBS well transforms AAS-NSs into the zeolite-NSs using the same SDAs as bulk synthesis. These results imply that this method enables us to synthesize almost all types of zeolite-NSs. NSs are optimal shape using zeolite catalytic membrane reactors because the thickness of the membrane is an important factor of the catalytic membrane reactor. We expect this combinatorial synthesis method to apply to other zeolites: e.g., nanoparticles, nanowires and nanorods. Moreover, the synthesized CHA-NSs have great potential for various applications such as a catalyst for methanol-to-olefins (MTO), cracking of polymers, and separation membrane because of their thickness and large external surface area.

Acknowledgements

The authors thank Prof. T. Hirai and Y. Shiraishi for their help with the use of the dynamic light scattering. The authors would like to thank Sachem, Inc. for their kind donation of the organic structure-direction agent (*N*,*N*,*N*-trimethyl-1-adamantanammonium hydroxide). This work was supported in part by Advanced Characterization Nanotechnology Platform, Nanotechnology Platform Program of the Ministry of Education, Culture, Sports, Science and Technology (MEXT), Japan, Grant Number JPMXP09A20OS0024 at the Research Center for Ultra-High Voltage Electron Microscopy (Nanotechnology Open Facilities) in Osaka University, and JSPS KAKENHI Grant Number JP20H05161, JP22H04477 and JP22J10688.

Conflict of Interest

The authors declare no conflict of interest.

Data Availability Statement

The data that support the findings of this study are available from the corresponding author upon reasonable request.

Keywords: Amorphous Aluminosilicate · Lamellar Phase · Nanosheets · Polymer Cracking · Zeolite

[1] M. Shamzhy, M. Opanasenko, P. Concepción, A. Martínez, *Chem. Soc. Rev.* **2019**, *48*, 1095–1149.
[2] A. Marcilla, A. Gómez-Siurana, D. Berenguer, *Appl. Catal. A* **2006**, *301*, 222–231.
[3] V. P. S. Caldeira, A. G. D. Santos, D. S. Oliveira, R. B. Lima, L. D. Souza, S. B. C. Pergher, *J. Therm. Anal. Calorim.* **2017**, *130*, 1939–1951.
[4] L. Tosheva, V. P. Valtchev, *Chem. Mater.* **2005**, *17*, 2494–2513.
[5] J.-M. Nhut, L. Pesant, J.-P. Tessonnier, G. Winé, J. Guille, C. Pham-Huu, M.-J. Ledoux, *Appl. Catal. A* **2003**, *254*, 345–363.
[6] A. Corma, V. Fornes, S. B. Pergher, T. L. M. Maesen, J. G. Buglass, *Nature* **1998**, *396*, 353–356.
[7] H. Y. Luo, L. Bui, W. R. Gunther, E. Min, Y. Román-Leshkov, *ACS Catal.* **2012**, *2*, 2695–2699.
[8] H. Zhang, Y. Ma, K. Song, Y. Zhang, Y. Tang, *J. Catal.* **2013**, *302*, 115–125.
[9] K. Varoon, X. Zhang, B. Elyassi, D. D. Brewer, M. Gettel, S. Kumar, J. A. Lee, S. Maheshwari, A. Mittal, C.-Y. Sung, M. Cococcioni, L. F. Francis, A. V. McCormick, K. A. Mkhoyan, M. Tsapatsis, *Science* **2011**, *334*, 72–75.
[10] P. Chlubná, W. J. Roth, H. F. Greer, W. Zhou, O. Shvets, A. Zukal, J. Čejka, R. E. Morris, *Chem. Mater.* **2013**, *25*, 542–547.
[11] M. Choi, K. Na, J. Kim, Y. Sakamoto, O. Terasaki, R. Ryoo, *Nature* **2009**, *461*, 246–249.
[12] S. Lin, L. Shi, T. Yu, *J. Phys. Chem. C* **2015**, *119*, 1008–1015.
[13] Y. Liu, N. Zhao, H. Xian, Q. Cheng, Y. Tan, N. Tsubaki, X. Li, *ACS Appl. Mater. Interfaces* **2015**, *7*, 8398–8403.
[14] T. Xue, H. Liu, Y. M. Wang, *RSC Adv.* **2015**, *5*, 12131–12138.
[15] W. Fu, Y. Feng, Z. Fang, Q. Chen, T. Tang, Q. Yu, T. Tang, *Chem. Commun.* **2016**, *52*, 3115–3118.
[16] Y. Luo, Z. Wang, S. Jin, B. Zhang, H. Sun, X. Yuan, W. Yang, *CrystEngComm* **2016**, *18*, 5611–5615.
[17] S. Zhu, S. Liang, Y. Wang, X. Zhang, F. Li, H. Lin, Z. Zhang, X. Wang, *Appl. Catal. B* **2016**, *187*, 11–18.
[18] P. Gong, B. Li, X. Kong, N. Wang, J. Liu, S. Zuo, *J. Mater. Sci.* **2017**, *52*, 9377–9390.
[19] F. Zhang, Y. Liu, Q. Sun, Z. Dai, H. Gies, Q. Wu, S. Pan, C. Bian, Z. Tian, X. Meng, Y. Zhang, X. Zou, X. Yi, A. Zheng, L. Wang, F.-S. Xiao, *Chem. Commun.* **2017**, *53*, 4942–4945.
[20] Y. Uchida, T. Nishizawa, T. Omiya, Y. Hirota, N. Nishiyama, *J. Am. Chem. Soc.* **2016**, *138*, 1103–1105.
[21] T. Omiya, K. Sasaki, Y. Uchida, N. Nishiyama, *ACS Appl. Nano Mater.* **2018**, *1*, 3779–3784.
[22] T. Omiya, K. Sasaki, Y. Uchida, N. Nishiyama, *Mol. Cryst. Liq. Cryst.* **2019**, *684*, 1–6.

[23] K. Sasaki, T. Okue, T. Nakai, Y. Uchida, N. Nishiyama, *Langmuir* **2021**, *37*, 5872–5877.
[24] K. Sasaki, T. Okue, Y. Shu, K. Miyake, Y. Uchida, N. Nishiyama, *Dalton Trans.* **2021**, *50*, 10394–10399.
[25] K. Sasaki, K. Miyake, Y. Uchida, N. Nishiyama, *ACS Appl. Nano Mater.* **2022**, *5*, 4998–5005.
[26] F. C. Larche, J. Appell, G. Porte, P. Bassereau, J. Marignan, *Phys. Rev. Lett.* **1986**, *56*, 1700–1703.
[27] W. Xu, J. Dong, J. Li, J. Li, F. Wu, *J. Chem. Soc. Chem. Commun.* **1990**, 755–756.
[28] Y. Hirota, K. Murata, S. Tanaka, N. Nishiyama, Y. Egashira, K. Ueyama, *Mater. Chem. Phys.* **2010**, *123*, 507–509.
[29] S. I. Zones, R. A. Van Nordstrand, *Zeolites* **1988**, *8*, 166–174.
[30] G. K. Williamson, W. H. Hall, *Acta Metall.* **1953**, *1*, 22–31.
[31] P. M. Ajayan, S. Iijima, *Philos. Mag. Lett.* **1992**, *65*, 43–48.
[32] N. Katada, Y. Kageyama, M. Niwa, *J. Phys. Chem. B* **2000**, *104*, 7561–7564.
[33] S. Kouva, J. Kanervo, F. Schüβler, R. Olindo, J. A. Lercher, O. Krause, *Chem. Eng. Sci.* **2013**, *89*, 40–48.
[34] Y. Higuchi, S. Miyagawa, S. Tanaka, *CrystEngComm* **2022**, *24*, 3859–3864.
[35] J. Felsche, S. Luger, C. Baerlocher, *Zeolites* **1986**, *6*, 367–372.
[36] N. Y. Chen, W. E. Garwood, *J. Catal.* **1978**, *52*, 453–458.

Manuscript received: December 17, 2021
Accepted manuscript online: September 22, 2022
Version of record online: October 17, 2022